Radiation Dosimetry of β-Amyloid Tracers ^{11}C-PiB and ^{18}F-BAY94-9172

Graeme J. O'Keefe[1], Timothy H. Saunder[1], Steven Ng[1], Uwe Ackerman[1], Henri J. Tochon-Danguy[1], J. Gordon Chan[1], Sylvia Gong[1], Thomas Dyrks[2], Stefanie Lindemann[2], Gerhard Holl[2], Ludger Dinkelborg[2], Victor Villemagne[1], and Christopher C. Rowe[1]

[1]Centre for Positron Emission Tomography, Austin Hospital, Heidelberg, Victoria, Australia; and [2]Bayer Schering Pharma, Berlin, Germany

β-Amyloid (Aβ) imaging has great potential to aid in the diagnosis of Alzheimer disease and the development of therapeutics. The radiation dosimetry of Aβ radioligands may influence their application; therefore, we calculated and compared the effective doses (EDs) of ^{11}C-PiB and a new ^{18}F-labeled ligand, ^{18}F-BAY94-9172. **Methods:** Attenuation-corrected whole-body scans were performed at 0, 15, 30, 45, and 60 min after injection of 350 ± 28 MBq (mean ± SD) of ^{11}C-PiB in 6 subjects and at 0, 20, 60, 120, and 180 min after injection of 319 ± 27 MBq of ^{18}F-BAY94-9172 in 3 subjects. Coregistered CT was used to define volumes of interest (VOIs) on the PET images. The source organs were the brain, lungs, liver, kidneys, spleen, and vertebrae. The VOIs for the contents of the gallbladder, urinary bladder, lower large intestine, upper large intestine, and small intestine were also defined. Total activity in each organ at each time point was calculated by use of reference organ volumes. The resultant time–activity curves were fitted with constrained exponential fits, and cumulated activities were determined. A dynamic bladder voiding model was used. The OLINDA/EXM program was used to calculate the whole-body EDs from the acquired data. **Results:** For ^{11}C-PiB, the highest absorbed doses were in the gallbladder wall (44.80 ± 29.30 μGy/MBq), urinary bladder wall (26.30 ± 8.50 μGy/MBq), liver (19.88 ± 3.58 μGy/MBq), and kidneys (12.92 ± 3.37 μGy/MBq). The ED was 5.29 ± 0.66 μSv/MBq. For ^{18}F-BAY94-9172, the highest doses were also in the gallbladder wall (132.40 ± 43.40 μGy/MBq), urinary bladder wall (24.77 ± 7.36 μGy/MBq), and liver (39.07 ± 8.31 μGy/MBq). The ED was 14.67 ± 1.39 μSv/MBq. **Conclusion:** The estimated organ doses for ^{11}C-PiB were comparable to those reported in earlier research. With the doses used in published studies (300–700 MBq), the EDs would range from 1.6 to 3.7 mSv. The ED of ^{18}F-BAY94-9172 was 30% lower than that of ^{18}F-FDG and, at the published dose of 300 MBq, would yield an ED of 4.4 mSv. The dosimetry of both Aβ radioligands is suitable for clinical and research applications.

Key Words: PET; radiation dosimetry; ^{11}C-PiB; ^{18}F-BAY94-9172

Amyloid plaques are one of the pathologic hallmarks of Alzheimer disease (AD). They consist of extracellular aggregates of β-amyloid (Aβ) (1,2) peptide that have diameters of about 50–100 μm and that are intimately surrounded by dystrophic axons and dendrites, reactive astrocytes, and activated microglia (3).

Several hypotheses have been postulated to explain the molecular mechanisms leading to AD (4,5), but the Aβ theory is the dominant etiologic paradigm at this time (2). The hypothesis states that an imbalance between the production and the removal of Aβ leads to its progressive accumulation and resultant synaptic dysfunction and neuronal loss, clinically manifested as a loss of cognitive functions (6,7). New treatment strategies for AD are aimed at delaying disease onset or slowing disease progression, through either preventing the deposition of Aβ or increasing the solubilization of Aβ. Given that these treatments are currently in trials, there is an urgent need for early disease recognition (8–10).

Amyloid imaging with PET is allowing new insights into Aβ deposition in the brain. "Pittsburgh Compound-B," or ^{11}C-PiB, is the most widely used PET radioligand for assessing Aβ in the brain (11–13). However, the 20.4-min radioactive half-life of ^{11}C restricts the use of PiB to PET centers with an on-site cyclotron and extensive radiochemistry infrastructure. Each patient dose requires a cyclotron run and radiosynthesis of ^{11}C-PiB immediately before the scan. An ^{18}F-labeled Aβ tracer is needed to permit wider application of amyloid imaging. [18]F has a 109.4-min half-life, so that a single large production should permit multiple scans to be performed at multiple PET sites, as is currently the case with ^{18}F-FDG imaging.

We have evaluated a novel ^{18}F-labeled tracer developed by Zhang et al. at the University of Pennsylvania (14). The tracer, ^{18}F-BAY94-9172, is a stilbene derivative that has shown high affinity and specificity for Aβ in vitro and binding to amyloid plaques but not neurofibrillary tangles in postmortem human brain tissue (14). In a proof-of-concept study in 35 subjects, ^{18}F-BAY94-9172 PET images were able to reliably distinguish subjects with AD from

healthy elderly subjects and subjects with frontotemporal dementia (11).

The aim of this study was to calculate the dosimetry of ^{11}C-PiB and ^{18}F-BAY94-9172 in healthy elderly control subjects to assess safety and suitability for clinical application from a radiodosimetric perspective.

MATERIALS AND METHODS

Subjects

Nine healthy control subjects were recruited, 6 for the ^{11}C-PiB protocol and 3 for the ^{18}F-BAY94-9172 protocol. Details for the subjects recruited and for the 2 protocols are given in Table 1. Subjects were assessed by neuropsychological testing and physical examination. This study was approved by the Austin Health Human Research Ethics Committee, and informed consent was obtained from all subjects before the imaging studies.

Radiosynthesis

[11]C-PiB and ^{18}F-BAY94-9172 were synthesized by use of ^{11}C and ^{18}F produced with an in-house 10-MeV cyclotron (Ion Beam Applications SA).

For ^{11}C-PiB synthesis, ^{11}C-6-OH-benzothiazole (BTA)-1 was produced in a one-step reaction of ^{11}C-methyl triflate (15–17) with the 6-OH-BTA-0 precursor. The product was reformulated with the Sep-Pak (Waters) method and filtered. The radioligand purity averaged 99%, and the specific radioactivity averaged 18 GBq/μmol.

^{18}F-BAY94-9172 was produced from the PEGN3-OMs (methyl-sulfonate) precursor and purified with a semipreparative column by the method of Zhang et al. (14). The product was reformulated with the Sep-Pak method. The radioligand purity averaged 96.0%, and the specific radioactivity averaged 140.5 GBq/μmol.

PET Protocol

Serial PET was performed with either a Philips Gemini/GS2 PET/CT scanner or a Philips Allegro dedicated PET scanner. Both systems are germanium oxyorthosilicate 3-dimensional scanners and have identical physical characteristics: an axial field of view of 180 mm, 45 image slices, a slice thickness of 4 mm, and a central spatial resolution of 5 mm full width at half maximum.

All subjects underwent whole-body (WB) low-dose CT (ldCT) with the Gemini PET/CT scanner. PET images were then acquired with the Gemini PET/CT scanner for the ^{11}C-PiB studies and the Allegro dedicated PET scanner for the ^{18}F-BAY94-9172 studies. In both cases, ldCT was used for anatomic localization to define

volumes of interest (VOIs) for subsequent dosimetric analysis. For the ^{11}C-PiB scans, ldCT was additionally used for attenuation correction of the PET emission scans. Before the ^{18}F-BAY94-9172 WB scans with the Allegro camera, an attenuation correction scan was acquired by use of a ^{137}Cs rotating point source with the Allegro camera.

Subjects were scanned in the supine position with the arms down. For the purposes of this study, a WB scan included the area from the top of the subject's head to the groin and ranged from 880 to 1,020 mm in axial extent. After a planning CT scan, a single WB ldCT scan was acquired with 30 mAs per slice and a 0.5-s rotation time. Subjects then underwent 5 consecutive WB scans. Each WB scan consisted of 10 or 11 bed positions with 1 min of acquisition time per bed position. Subjects were permitted to leave the scanner between the third and fourth and between the fourth and fifth ^{18}F-BAY94-9172 WB scans. Additional attenuation correction scans were acquired with a ^{137}Cs rotating point source before the fourth and fifth WB scans. The imaging sequences for ^{11}C-PiB and ^{18}F-BAY94-9172 are described in Table 2. For both ^{11}C-PiB scanning and ^{18}F-BAY94-9172 scanning, a standard cylindric source of activity (with an activity of 5 MBq and a volume of 5 mL) was placed opposite the subject's head for calibration confirmation purposes.

PET Data Analysis

The Gemini and Allegro scans were reconstructed with the RAMLA-3D algorithm after being corrected for attenuation, dead time, half-life decay, and scatter with the single-scatter simulation (SSS) correction (18). PET images were generated with an image size of 144×144 per slice and a voxel size of $4 \times 4 \times 4$ mm^3. For scans acquired with the Allegro scanner, the reconstructed images were retrospectively coregistered with ldCT. All images were reconstructed with standardized uptake value (SUV) units that were defined as

$$SUV = \frac{C(t) \times 2^{t/\tau_{1/2}}}{D/M_{body}}, \qquad \text{Eq. 1}$$

where $C(t)$ is the voxel radioactivity concentration (kBq/mL) at time t after injection, $\tau_{1/2}$ is the isotope decay half-life, D is the injected dose (MBq), and M_{body} (kg) is the mass of the subject.

The camera sensitivity is calibrated on a quarterly basis with a uniform cylindric phantom (dimensions: diameter, 20 cm; length, 30 cm; and volume, 9,420 mL) filled with a well counter–calibrated

TABLE 1. Subject Details and Injected Radioactivities of ^{11}C-PiB and ^{18}F-BAY94-9172

Tracer or parameter	Subject	Sex	Age (y)	Mass (kg)	Injected dose (MBq)
[11]C-PiB	1	F	63	68.5	370.1
	2	F	56	66.0	377.7
	3	F	70	61.0	363.9
	4	M	65	93.5	344.3
	5	M	64	79.0	300.2
	6	M	61	88.0	352.1
Mean ± SD			63.2 ± 4.2	76.0 ± 11.8	351.4 ± 25.4
^{18}F-BAY94-9172	1	M	63.5	101	299.3
	2	M	73.5	103	307.2
	3	F	63.1	66.9	349.5
Mean ± SD			66.7 ± 4.8	90.3 ± 16.6	318.7 ± 22.0

concentration of ^{18}F-FDG. A weekly validation of the calibration is performed with a uniform [68]Ge phantom (dimensions: diameter, 20 cm; length, 20 cm; and volume, 6,283 mL) that is cross-calibrated with respect to a calibrated ^{18}F-FDG source.

[11]C SUV Validation

In addition to the quarterly ^{18}F-FDG calibration and weekly [68]Ge validation, a ^{11}C-phantom validation was undertaken. The 9,420-mL phantom was filled with 370 MBq of ^{11}C-PiB, and images were acquired under conditions identical to those used for subject imaging. Three bed positions were used to encompass the entire phantom, and ldCT was used to allow CT-based attenuation correction. Five scans were acquired with a 1-min duration per bed position and starting acquisition times identical to those used for ^{11}C-PiB WB scanning (Table 2). After reconstruction with protocols identical to those used for WB reconstruction, representative circular regions of interest were defined, and mean SUVs were determined. The resultant mean SUVs were in agreement with the ^{18}F-FDG–based routine SUV calibration results.

Dosimetry

For both ^{11}C-PiB and ^{18}F-BAY94-9172, after reconstruction, VOIs were defined on the basis of ldCT. The organs defined by the ldCT VOI process were the brain, lungs, liver, kidneys, spleen, and vertebrae. For these organs, representative regions were defined on the basis of ldCT and, when applied to emission images, allowed the determination of the average SUV for an organ. Because representative regions of these organs were used, quantitation issues arising from effects, such as respiratory motion effects, on the dome of the liver and the partial volume at the boundary of organs were minimized. By use of the known mass of an organ or its contents, the mean SUV could be converted to percentage injected radioactivity, as expressed in Equation 2.

For organs in which the radioactivity of the contents was considered, such as the gallbladder, urinary bladder, lower large intestine, upper large intestine, and small intestine, VOIs were defined on the basis of dynamic PET emission images.

The VOIs for organs and organ contents were then applied to the coregistered PET images from which the mean SUV was determined. The activity in each organ was then determined by half-life decaying the SUV followed by scaling by the ratio of the reference man (19) organ mass or organ content volume to that of the study subject body mass as is represented in Equation 2. This procedure provided an estimate of the activity present in a reference man organ at time t for the appropriate tracer. By repeating this analysis for each time point, we obtained a time–activity curve for a standardized organ; the data were expressed as percentage injected radioactive dose (%IRD) (as distinct from %ID, which generally refers to percentage injected pharmacologic dose), as follows:

$$\%IRD_{organ}(t) = \overline{SUV}_{organ}(t) \times 2^{-t/\tau_{1/2}} \times \frac{M_{organ}}{M_{body}} \times 100, \quad \text{Eq. 2}$$

where $\%IRD_{organ}(t)$ and $\overline{SUV}_{organ}(t)$ are, respectively, the %IRD and the mean SUV of the organ of interest determined at time t after injection and M_{organ} is the mass of the organ of interest.

The cumulated activity of the urinary bladder contents was determined by fitting the time–activity curve for the bladder contents with an exponential in-growth function of the form

$$U(t) = U(0) \times (1 - e^{-t/\tau}), \quad \text{Eq. 3}$$

where $U(t)$ is the fraction of activity in the bladder at time t after injection and τ is the isotope half-time (where $\tau = \tau_{1/2}/\ln2$). These parameters were entered into the bladder voiding model module of OLINDA/EXM (20) with a voiding interval of 2.4 h.

The OLINDA/EXM application developed by Stabin et al. (20) was used to determine the effective doses (EDs) for individual organs on the basis of the set of source organs defined in the organ markup stage. Stabin et al. introduced the concept of cumulated activity, as opposed to the MIRDOSE concept of residence time (21). In the framework of Stabin et al., the dose absorbed by a target organ, denoted as r_k, is expressed as

$$D(r_k) = \sum_h N_h \times S(r_k \leftarrow r_h), \quad \text{Eq. 4}$$

where $S(r_k \leftarrow r_h)$ (21) is the S factor (which Stabin et al. (20) referred to as the dose fraction), which is the fraction of the dose absorbed by the target organ (r_k) from radiation emitted by the source organ (r_h). The number of disintegrations occurring in the source organ (N_h) was referred to by Stabin et al. as the cumulated activity in that organ.

For both ^{11}C-PiB and ^{18}F-BAY94-9172, constrained monoexponential fits were applied to the standardized organ %IRD time–activity curves to allow parametric calculation of cumulated activities.

For determination of the cumulated activity of the gallbladder contents, the area under the curve (AUC) was calculated from the available time–activity curve via the trapezoidal rule method. After the final imaging time point, when a single exponential decay function with a half-life equal to the physical decay constant is applied, it is assumed that there is no further excretion and that clearance occurs only through the physical decay of the isotope.

The resultant reference man–normalized cumulated activities were entered into OLINDA/EXM as source organs from which the EDs were calculated for a range of sources or target organs by use of MIRD methods (22,23). The radiation transport phantom selected from OLINDA/EXM was the hermaphroditic phantom, which is based on the measurements of Cristy and Eckerman (24) for a 73.7-kg adult phantom but nominally refers to the 70-kg adult phantom from ICRP Publication 23 (19). As a result, the radiation dose estimates were considered to apply to both male and female subjects with a body weight of 73.7 kg.

RESULTS

WB coronal projections of a subject infused with ^{11}C-PiB are shown in Figure 1. It is visually evident that there were high levels of accumulation of ^{11}C-PiB in the liver, gallbladder, and urinary bladder and significant levels of accumulation in the kidneys, spleen, and upper large intestine. Similar patterns of uptake in the liver, urinary bladder, and upper large intestine were observed for ^{18}F-BAY94-9172, as shown in Figure 2. In addition, compared with ^{11}C-PiB, for ^{18}F-BAY94-9172, there was evidence of higher levels of uptake in the spleen as well as in the lower large intestine and small intestine, as shown in Figure 3.

Cumulated activities were determined for individual subjects to allow individualized dose estimates to be determined. Measures of the reproducibility of cumulated activities after reference man organ normalization for both ^{11}C-PiB and ^{18}F-BAY94-9172 are shown in Figures 4 and 5, respectively; these figures show the population-averaged %IRD time–activity curves. The data for the subset of organs shown demonstrated good reproducibility, with the bladder contents showing the greatest variation, particularly for ^{18}F-BAY94-9172; in that study, subjects had the opportunity to void the urinary bladder. The large variability in bladder content measurements shown for ^{18}F-BAY94-9172 in Figure 5 could be addressed with a more rigorous bladder voiding regimen and a sample size larger than the sample size of 3 used in the present study.

The OLINDA/EXM results for ^{11}C-PiB and ^{18}F-BAY94-9172 are shown in Table 3, along with the EDs reported by
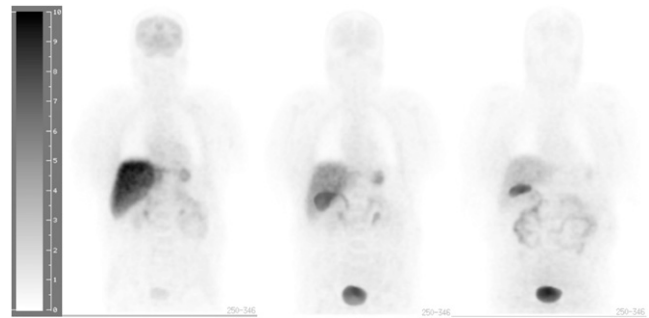
FIGURE 2. Coronal projections (100 mm thick) of 3 sequential WB images (0, 60, and 180 min after injection of ^{18}F-BAY94-9172) of subject 1. Images are displayed on SUV scale, giving indication of differences in %IRDs.

the ICRP Publication 60 (25). Table 3 shows the ^{11}C-PiB organ dosimetry for the 6 subjects for whom the ED was determined 5.29 ± 0.66 μSv/MBq (mean ± SD). The organs receiving the highest absorbed doses were the gallbladder wall (44.80 ± 29.30 μGy/MBq), urinary bladder wall (26.30 ± 8.50 μGy/MBq), liver (19.88 ± 3.58 μGy/MBq), and kidneys (12.92 ± 3.37 μGy/MBq).

Table 3 shows the ^{18}F-BAY94-9172 organ dosimetry for the 3 subjects for whom the ED was determined to be 14.67 ± 1.39 μSv/MBq. As with ^{11}C-PiB, the organs receiving the highest doses were the gallbladder wall (132.40 ± 43.40 μGy/MBq), urinary bladder wall (24.77 ± 7.36 μGy/MBq), and liver (39.07 ± 8.31 μGy/MBq).

DISCUSSION

As anticipated, the organ and WB EDs for ^{11}C-PiB were substantially lower than those for ^{18}F-BAY94-9172 because of the much shorter decay half-life of [11]C (20.4 min) than of [18]F (109.8 min). Both tracers showed substantial clearance through the liver and excretion of radioactivity into the bowel. Both tracers also showed considerable renal excretion, so that the data for the critical organs (i.e., gallbladder wall, liver, and urinary bladder wall) were the
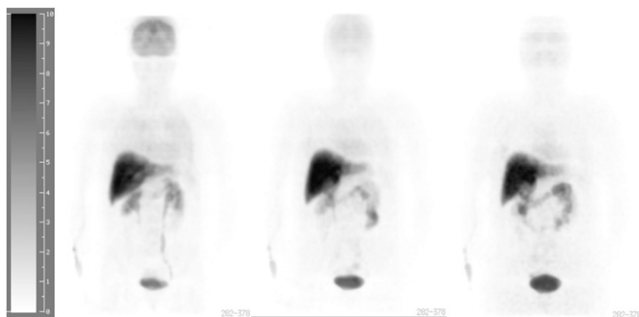
FIGURE 1. Coronal projections (100 mm thick) of 3 sequential WB images (0, 30, and 60 min after injection of ^{11}C-PiB) of subject 1. Images are displayed on SUV scale (range, 0–10), giving indication of differences in %IRDs.
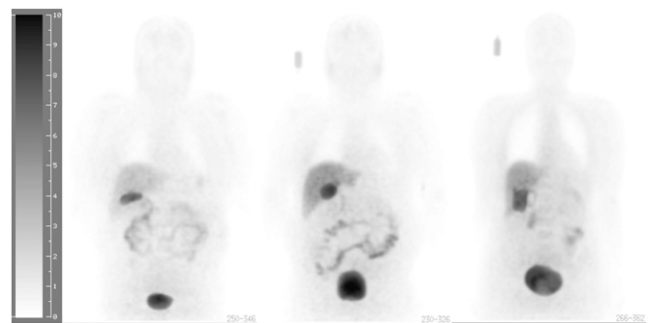
FIGURE 3. Coronal projections (100 mm thick) of WB images of 3 subjects 3 h after injection with ^{18}F-BAY94-9172, illustrating variable levels of radioactivity in contents of large intestine.
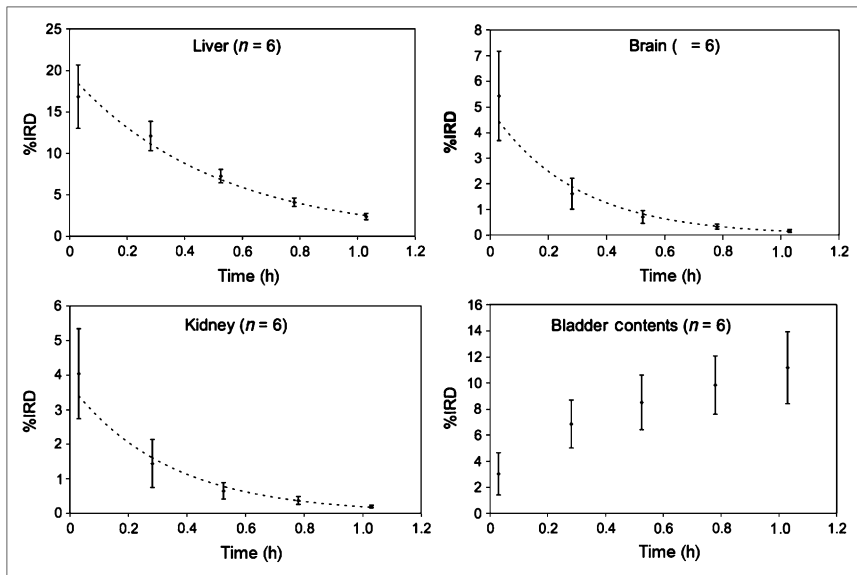
FIGURE 4. ^{11}C-PiB time–activity curves for liver, brain, kidneys, and bladder contents, expressed as %IRD normalized to reference man (*19*). Variability represented by error bars resulted from differences in individual subjects, placement of regions of interest, and emission image statistics.

same. However, a relatively high radioactive dose of ^{11}C-PiB (typically 555 MBq) is recommended to yield reasonable image quality at the time of acquisition, between 40 and 70 min after injection (2–3.5 half-lives after injection for ^{11}C). Thus, the WB ED for the recommended dose of ^{11}C-PiB is 2.9 mSv. The optimal imaging time for ^{18}F-BAY94-9172 is between 90 and 120 min after injection (0.8–1.1 half-lives for ^{18}F), and excellent results have been achieved with 300 MBq (*11*) at this time point. This dose of ^{18}F-BAY94-9172 yields a WB ED of 4.4 mSv.

Scheinin et al. (*26*) previously studied ^{11}C-PiB radiation dosimetry in humans by using a different methodology. In the present study, time–activity curves were determined for each individual across the entire body and then used to calculate the dosimetry for each individual. In contrast,

Scheinin et al. (*26*) determined averaged time–activity curves by scanning different sets of subjects for different anatomic regions with 2 different PET scanners. Results were then scaled to the reference man, and an ED was determined. There was generally good agreement between the data of Scheinin et al. (*26*) and those in the present study, as summarized in Table 4.

Table 5 summarizes the EDs of other common ^{18}F-radiopharmaceuticals, ^{18}F-BAY94-9172, and ^{11}C-PiB. The ED of ^{18}F-BAY94-9172 was generally somewhat lower than the EDs of the other ^{18}F-labeled radiopharmaceuticals, as the organs with the highest ^{18}F-BAY94-9172 uptake had relatively low radiosensitivity.

The radiation doses from diagnostic levels of infused activities of ^{11}C-PiB make it well suited to serial studies, but
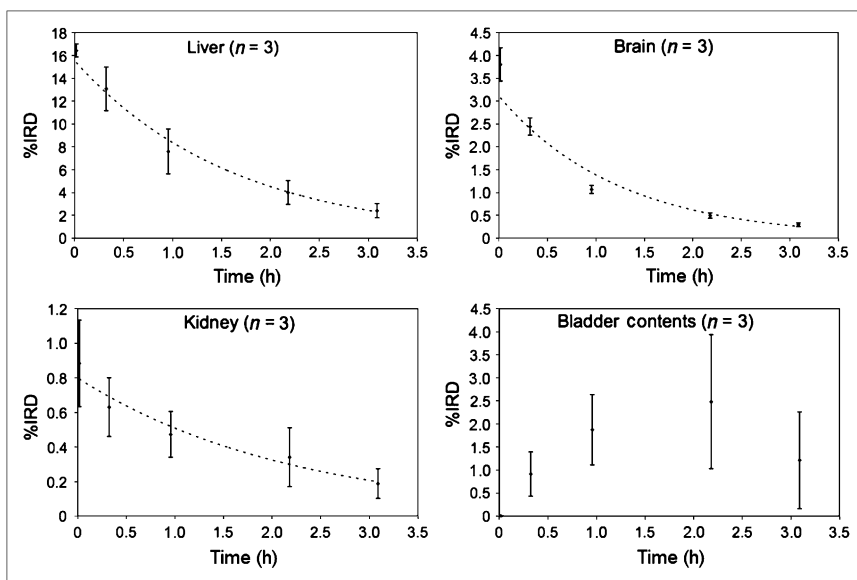

FIGURE 5. ^{18}F-BAY94-9172 time–activity curves for liver, brain, kidneys, and bladder contents, expressed as %IRD normalized to reference man (*19*). Variability represented by error bars resulted from differences in individual subjects, placement of regions of interest, and emission image statistics. High variability in bladder contents illustrated different patterns of individual bladder voiding.

TABLE 3. ^{11}C-PiB and ^{18}F-BAY94-9172 Radiation Doses Determined With 73.7-kg Hermaphroditic Adult Phantom

Organ or parameter	Mean ± SD dose of:	
	^{11}C-PiB (n = 6)	^{18}F-BAY94-9172 (n = 3)
Adrenal glands	4.00 ± 0.32	15.30 ± 1.56
Brain	3.92 ± 1.44	10.28 ± 1.55
Breasts	2.21 ± 0.23	9.05 ± 0.56
Gallbladder wall	44.80 ± 29.30	132.40 ± 43.40
Lower large intestine wall	3.10 ± 0.35	15.73 ± 0.61
Small intestine	4.65 ± 0.74	14.03 ± 0.42
Stomach wall	3.11 ± 0.28	13.20 ± 1.04
Upper large intestine wall	3.87 ± 0.43	17.83 ± 2.18
Heart wall	3.24 ± 0.34	12.90 ± 0.96
Kidneys	12.92 ± 3.37	20.03 ± 5.59
Liver	19.88 ± 3.58	39.07 ± 8.31
Lungs	6.59 ± 3.31	8.26 ± 0.56
Muscle	2.57 ± 0.24	10.90 ± 0.66
Ovaries	3.21 ± 0.33	13.70 ± 0.80
Pancreas	4.02 ± 0.33	15.93 ± 1.63
Red marrow	2.43 ± 0.20	18.93 ± 4.28
Osteogenic cells	3.60 ± 0.48	22.03 ± 4.16
Skin	1.98 ± 0.20	8.38 ± 0.43
Spleen	4.03 ± 0.57	15.13 ± 7.02
Testes	2.12 ± 0.10	10.06 ± 5.82
Thymus	2.54 ± 0.31	11.07 ± 0.80
Thyroid	2.24 ± 0.21	10.47 ± 0.35
Urinary bladder wall	26.30 ± 8.50	24.77 ± 7.36
Uterus	3.73 ± 0.42	13.83 ± 0.90
Total body	3.23 ± 0.30	12.23 ± 0.95
ED equivalent (μSv/MBq)	8.93 ± 1.80	23.17 ± 4.29
ED (μSv/MBq)	5.29 ± 0.66	14.67 ± 1.39

Data are reported in μGy/MBq unless otherwise indicated.

TABLE 5. Comparison of ED (Adult Phantom Model) Estimates for ^{11}C-PiB, ^{18}F-BAY94-9172, and Other ^{18}F-Labeled Pharmaceuticals

Tracer (study)	ED (μSv/MBq)
^{11}C-PiB	5.29 ± 0.66
^{11}C-PiB (26)	4.74
^{18}F-BAY94-9172	14.67 ± 1.39
^{18}F-FDG (22,23)	19.0
^{18}F-A85380 (27)	19.4
^{99m}Tc-phosphonate* (23)	5.7

*Common SPECT agent.

of ^{11}C-PiB, the longer physical half-life of ^{18}F-BAY94-9172 than of ^{11}C-PiB is an advantage for multicenter studies and widespread clinical use.

CONCLUSION

The radiation dosimetry for amyloid imaging agents ^{11}C-PiB and ^{18}F-BAY94-9172 has been calculated; the EDs are 5.29 ± 0.66 μSv/MBq and 14.67 ± 1.39 μSv/MBq, respectively. The calculated ED of ^{11}C-PiB is in good agreement with a previous measurement made by Scheinin et al. (26). With diagnostic imaging dose levels of 550 MBq for ^{11}C-PiB and 350 MBq for ^{18}F-BAY94-9172, the radiation doses of ^{11}C-PiB and ^{18}F-BAY94-9172 will be 1.85 and 5.13 mSv, respectively.

the short physical half-life of ^{11}C, which requires individual dose production immediately before use, is a disadvantage. The ED of ^{18}F-BAY94-9172 is somewhat lower than that of ^{18}F-FDG; with judicious selection of infused activities, ^{18}F-BAY94-9172 may be suitable for serial studies. Some restrictions on the number of ^{18}F-BAY94-9172 studies performed per year on healthy subjects will be needed to comply with radiation protection guidelines for research subjects. Although the ED of ^{18}F-BAY94-9172 is almost 3 times higher than that

TABLE 4. Comparison of ^{11}C-PiB Dosimetry from Scheinin et al. (26) and Present Study

Organ	μGy/MBq from:	
	Scheinin et al.	Present study
Gallbladder wall	41.5	44.80 ± 29.30
Urinary bladder wall	16.6	26.30 ± 8.50
Liver	19.0	19.88 ± 3.58
Kidney	12.6	12.92 ± 3.37
Upper large intestine wall	9.0	3.87 ± 0.43

REFERENCES

1. Masters C, Simms G, Weinman N, Multhaup G, McDonald B, Byreuther K. Amyloid plaque core protein in Alzheimer disease and Down syndrome. *Proc Natl Acad Sci USA.* 1985;82:4245–4249.
2. Masters CL, Cappai R, Barnham KJ, Villemagne VL. Molecular mechanisms for Alzheimer's disease: implications for neuroimaging and therapeutics. *J Neurochem.* 2006;97:1700–1725.
3. Jellinger K, Bancher C. Neuropathology of Alzheimer's disease: a critical update. *J Neural Transm Suppl.* 1998;54:77–95.
4. Selkoe D. The genetics and molecular pathology of Alzheimer's disease: roles of amyloid and presenilins. *Neurol Clin.* 2000;18:903–922.
5. Bartus R, Emerich D. Cholinergic markers in Alzheimer disease. *JAMA.* 1999; 282:2208–2209.
6. Selkoe D. Alzheimer's disease: genes, proteins and therapy. *Physiol Rev.* 2001; 81:741–766.
7. Masters C. Alzheimer's disease. *BMJ.* 1998;316:446–448.
8. Schenk D, Hagen M, Seubert P. Current progress in beta-amyloid immunotherapy. *Curr Opin Immunol.* 2004;16:599–606.
9. Ritchie CW, Bush AI, Mackinnon A, et al. Metal-protein attenuation with iodochlorhydroxyquin (clioquinol) targeting Abeta amyloid deposition and toxicity in Alzheimer disease: a pilot phase 2 clinical trial. *Arch Neurol.* 2003;60:1685–1691.

10. Xia W. Amyloid inhibitors and Alzheimer's disease. *Curr Opin Investig Drugs.* 2003;4:55–89.

11. Rowe C, Ackerman U, Browne W, et al. Imaging of amyloid beta in Alzheimer's disease with ^{18}F-BAY94-9172. *Lancet Neurol.* 2008;7:129–135.

12. Rowe C, Ng S, Ackerman U, et al. Imaging beta-amyloid burden in ageing and dementia. *Neurology.* 2007;68:1718–1725.

13. Pike K, Savage G, Villemagne V, et al. Beta-amyloid imaging and memory in nondemented individuals: evidence for preclinical Alzheimer's disease. *Brain.* 2007;130:2837–2844.

14. Zhang W, Oya S, Kung M-P, Hou C, Maier DL, Kung HF. F-18 stilbenes as PET imaging agents for detecting beta-amyloid plaques in the brain. *J Med Chem.* 2005;48:5980–5988.

15. Wilson AA, Garcia A, Chestakova A, Kung H, Houle S. A rapid one-step radiosynthesis of the β-amyloid imaging radiotracer *N*-methyl-[^{11}C]2(40-methylaminophenyl)-6-hydroxybenzothiazole ([^{11}C]-6-OH-BTA-1). *J Labelled Comp Radiopharm.* 2004;47:679–682.

16. Mathis CA, Wang Y, Holt DP, Huang GF, Debnath ML, Klunk WE. Synthesis and evaluation of ^{11}C-labeled 6-substituted 2-arylbenzothiazoles as amyloid imaging agents. *J Med Chem.* 2003;46:2740–2754.

17. Price JC, Klunk WE, Lopresti BJ, et al. Kinetic modeling of amyloid binding in humans using PET imaging and Pittsburgh Compound-B. *J Cereb Blood Flow Metab.* 2005;25:1528–1547.

18. Accorsi R, Adam LE, Werner ME, Karp JS. Implementation of a single scatter simulation algorithm for 3D PET: application to emission and transmission scanning. *Nuclear Science Symposium Conference Record, 2002 IEEE.* 2002; 2: 816–820.

19. International Commission on Radiological Protection. *Report of the Task Group on Reference Man.* Oxford, U.K.: Pergamon Press; 1975. ICRP Publication 23.

20. Stabin MG, Sparks RB, Crowe E. OLINDA/EXM: the second-generation personal computer software for internal dose assessment in nuclear medicine. *J Nucl Med.* 2005;46:1023–1027.

21. Loevinger R, Budinger T, Watson E. *MIRD Primer for Absorbed Dose Calculations.* Reston, VA: Society of Nuclear Medicine; 1988.

22. International Commission on Radiological Protection. *Radiation Dose to Patients from Radiopharmaceuticals.* Oxford, U.K.: Pergamon Press; 1987. ICRP Publication 53.

23. International Commission on Radiological Protection. *Radiation Dose to Patients from Radiopharmaceuticals.* Oxford, U.K.: Pergamon Press; 1998. ICRP Publication 80: Addendum 2 to Publication 53.

24. Cristy M, Eckerman KF. *Specific Absorbed Fractions of Energy at Various Ages from Internal Photon Sources. VII. Adult Male.* Oak Ridge, TN: Oak Ridge National Laboratory; 1987. Document Number ORNL/TM-8381/V7.

25. International Commission on Radiological Protection. *Recommendations of the International Commission on Radiological Protection.* Oxford, U.K.: Pergamon Press; 1991. ICRP Publication 60.

26. Scheinin NM, Tolvanen TK, Wilson IA, Arponen EM, Nagren KA, Rinne JO. Biodistribution and radiation dosimetry of the amyloid imaging agent ^{11}C-PIB in humans. *J Nucl Med.* 2007;48:128–133.

27. Bottlaender M, Valette H, Roumenov D, et al. Biodistribution and radiation dosimetry of ^{18}F-fluoro-A85380 in healthy volunteers. *J Nucl Med.* 2003;44: 596–601.